Origin of and deformation related to the Rimae Doppelmayer on the Moon

The optical stereo-images (5 m/pixel resolution) captured by the Terrain Mapping Camera-2 (TMC-2) on board the Chandrayaan-2 Lunar orbiter[1] and digital elevation models (10 m/pixel resolution prepared from these images) help understand the morphology of the structural features on the surface of the Moon.

The Rimae Doppelmayer (RD) within the Mare Humorum in the nearside of the Moon is a NNW–SSE-trending, ~130 km long graben system (Figure 1 *a* and *b*). The topographic profiles across the RD resemble those of typical lunar grabens[2,3] (Figure 1 *c*). Despite its prominent presence in the available images of the Moon, detailed morphometric studies of the RD are lacking. The very high-resolution TMC-2 image of this graben system, though a partial coverage of its length, has provided an opportunity for morphometric estimates to understand and quantify the crustal deformation related to this graben and also the age of its formation.

The Mare Humorum is Nectarian in age with low titanium basalts[4], mainly pigeonite- and augite-rich[5], and belonging to the Imbrian–Eratosthenian periods[6,7]. Compressional features such as wrinkle ridges, lobate scarps and extensional features such as grabens and collapsed lava tubes/rilles are common in the basin. The rilles and grabens are proposed to be a combined effect of dykes and extensional faulting beneath the mare. Rilles are also assumed to be positioned as hinge areas of tilting or subsiding basins[6].

TMC-2 has photographed the southern 30 km of the NNW–SSE-trending RD (Figure 1 *a*(ii)). In the present study, age extension across the RD and longitudinal strain was estimated using the TMC-2 image. Age has been estimated by the crater size frequency distribution method[8] using the buffered crater counting technique, with 1.5 times the crater radius[9]. The CraterTools add-on in ArcGIS was used for the crater size–frequency measurements, whereas CraterStats II was used for age determination. Crater statistics obtained by crater counting was fitted with the crater production function for the Moon and to deduce the absolute age, crater frequency for certain crater sizes was combined with the chronology function for the Moon[10]. Craters present on the graben floor may be older than the event of graben formation and, therefore, were not considered for age estimation. Extension across the RD and the longitudinal strain accumulated were estimated using established formulae related to the graben morphology[11,12]

$$\text{Total extension } (D) = d1/\tan\alpha_1 + d2/\tan\alpha_2, \quad (1)$$

where $d1$, $d2$ are the graben depths on two sides and α_1, α_2 are the dip angle of the graben (considered as 60° in the absence of subsurface data[13]) (Figure 1 *b*).

$$\text{Regional longitudinal strain } (e_{reg}) \text{ along the profile} = D/L_0, \quad (2)$$

where D is the total extension and L_0 is the original length of the profile (Figure 1 *b*).

Extension across the graben ranged from 81 to 344 m, with an average of 188.4 m (Table 1). The regional longitudinal strain was between 0.07 and 0.27, with an average of 0.14 (Table 1). The age of the RD was estimated to be ~1.9 Ma (Figure 2 *a* and *b*). This deformation corroborates with those of other studies on recent geological activities like faulting and moonquakes[14,15]. Near the RD, volcanic domes and a ~NE–SW-trending prominent lobate scarp oblique to it are present[16] (Figure 1 *a*(i)). However, the absence of any convincing arcuate or radial fractures in the immediate vicinity of the volcanic domes suggests that the origin of the RD was not influenced by volcanic

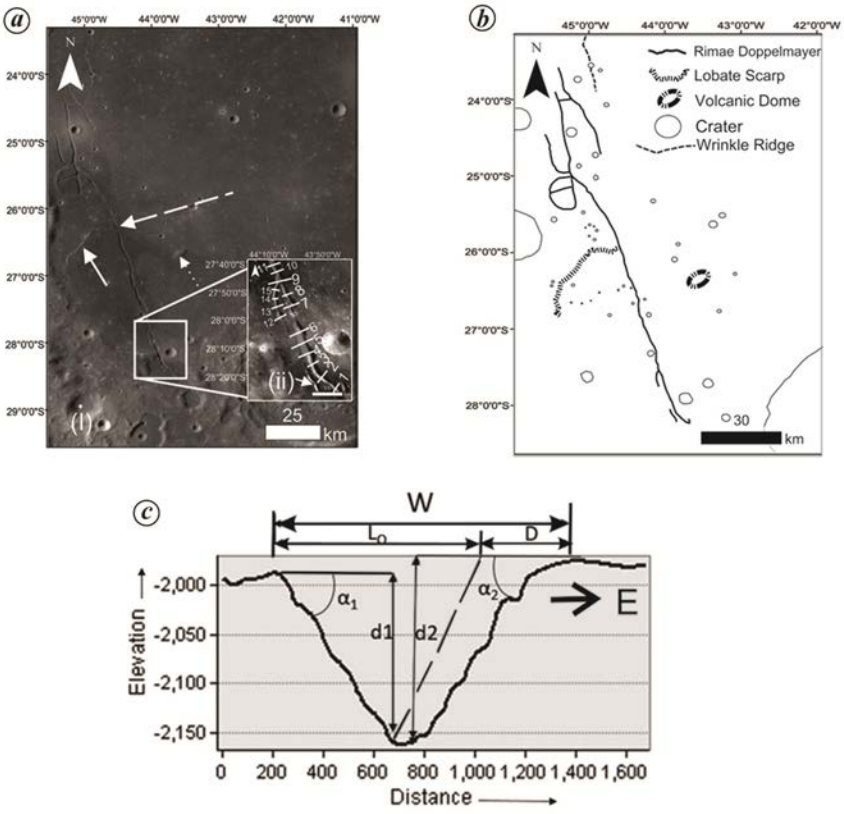

Figure 1. ***a***, (i) LROC WAC image of the Rimae Doppelmayer (RD) on the Moon (indicated by the broken white arrow) and a lobate scarp (indicated by white solid arrow) oblique to it within the Mare Humorum, a volcanic dome to the east of the RD marked by the dotted arrow (almost at the central part of the image) (image ID: Lunar_LRO_LROC-WAC_Mosaic_global_100m_June2013 with 100 m/pixel resolution). (ii) Southern part of the RD. Numbered lines are traces of section planes. Arrows indicate relic pit craters (image ID: ch2_tmc_ndn_20200209T0032589097_d_oth_gds.tif). ***b***, Trace map of geomorphological features of the RD and its surroundings. ***c***, A representative topographic profile (profile 3) across the RD showing the parameters used in eqs (1) and (2)[15].

Table 1. Detailed data generated for morphometric analysis of the Rimae Doppelmayer (see Figure 1 *a*(i) and *b*)

Section no.	*d1* (graben depth) (m)	*d2* (graben depth) (m)	Dip angle (deg)[15]	*d1*/tan 60	*d2*/tan 60	*D* (total extension) (m)	L_0 (original length of profile) (m)	e_{reg} (longitudinal strain)
1	169	183	60	97.57	105.65	203	1197	0.169
2	256	267	60	147.806	154.157	302	1098	0.275
3	183	195	60	105.6582	112.5866	218	1682	0.129
4	296	300	60	170.9007	173.2102	344	1906	0.180
5	240	100	60	138.5681	57.73672	196	1845	0.106
6	288	267	60	166.2818	154.157	320	2089	0.153
7	190	175	60	109.6998	101.0393	211	1547	0.136
8	134	115	60	77.36721	66.39723	144	1064	0.135
9	137	84	60	79.09931	48.49885	128	1669	0.076
10	110	60	60	63.51039	34.64203	98	1402	0.07
11	145	105	60	83.71824	60.62356	144	1645	0.087
12	164	157	60	94.68822	90.64665	185	1182	0.156
13	80	60	60	46.18938	34.64203	81	719	0.112
14	119	107	60	68.7067	61.77829	130	950	0.137
15	120	92	60	69.28406	53.11778	122	678	0.180

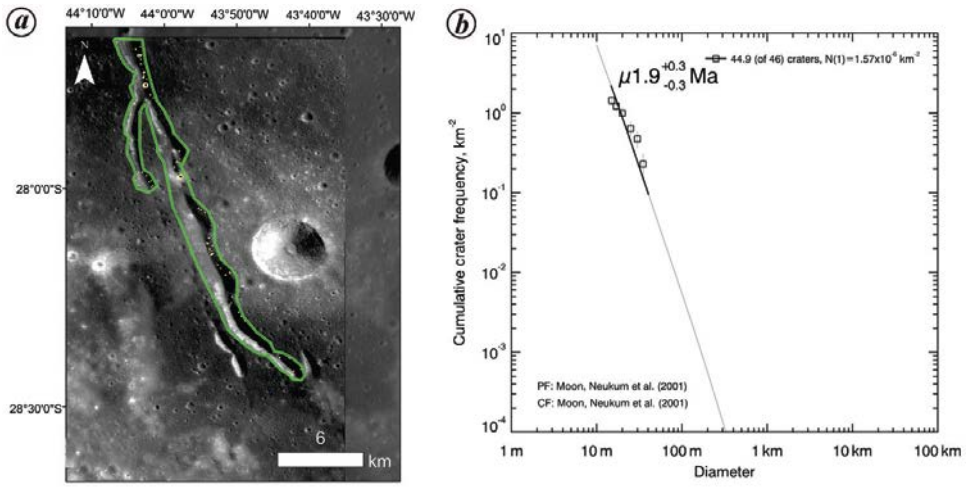

Figure 2. ***a***, Buffer crater count on the RD (image ID: ch2_tmc_ndn_20200209T0032589097_d_oth_gds.tif). ***b***, Crater size–frequency distribution and derived model age of the graben in CraterStats-II (cumulative fit).

doming. Some of the lunar grabens are proposed to have formed by extensional tectonic activities[17,18], often by local tension related to the formation of wrinkle ridges or lobate scarps in the vicinity[17]. Such grabens are at high angles to the wrinkle ridges and/or lobate scarps[17], depicting a subparallel trend to the maximum compressive stress and oblique to the minimum compressive stress/tensile stress. Grabens possibly also form due to ground subsidence along pit crater chains which are either related to extensional faulting or volcanism[17,19]. Expansion of the surface due to rising of dykes up to shallow depths is also often responsible for the formation of grabens[3,16]. The RD is a very recently formed structure (~1.9 Ma; Figure 2 *b*). Hence it is probably not related to the much older mare volcanism. The RD has prominent convex, outward, arcuate segments along the margin at its southern part (Figure 1 *a*(ii)). These arcuate segments are remnants of pit craters which might have initiated the collapse of the ground due to normal faulting triggered by the local stress field generated during the formation of the lobate scarp oblique to the RD. Therefore, from these preliminary observations and results, it is relevant to relate this graben to the collapse of a pit-crater chain.

1. Chowdhury, A. R. *et al.*, *Curr. Sci.*, 2020, **118**(4), 566; https://www.currentscience.ac.in/Volumes/118/04/0566.pdf.
2. Martin, E. S. and Watters, T. R., In AGU Fall Meeting Abstracts, 2018, vol. 2018, pp. P23D–3473.
3. Callihan, M. B. and Klimczak, C., *Lithosphere*, 2019, **11**(2), 294–305; https://doi.org/10.1130/L1025.1.
4. Pieters, C., Head, J. W., McCord, T. B., Adams, J. B. and Zisk, S., In Lunar and Planetary Science Conference Proceedings, Lunar and Planetary Institute, Houston, Texas, USA, 1975, vol. 6, pp. 2689–2710.
5. Thesniya, P. M. and Rajesh, V. J., *Planet. Space Sci.*, 2020, **193**, 105093; https://doi.org/10.1016/j.pss.2020.105093.
6. Ronca, L. B., *Icarus*, 1965, **4**(4), 390–395; https://doi.org/10.1016/0019-1035(65)900-42-4.
7. DeHon, R. A., In Lunar and Planetary Science Conference Proceedings, Lunar and Planetary Institute, Houston, Texas, USA, 1977, vol. 8, pp. 633–641.
8. Michael, G. G. and Neukum, G., *Earth Planet. Sci. Lett.*, 2010, **294**(3–4), 223–229; https://doi.org/10.1016/j.epsl.2009.12.041.
9. Kneissl, T., Michael, G. G., Platz, T. and Walter, S. H. G., *Icarus*, 2015, **250**, 384–394; https://doi.org/10.1016/j.icarus.2014.12.008.

10. Neukum, G., Ivanov, B. A. and Hartmann, W. K., In Chronology and Evolution of Mars. Space Sciences Series of ISSI (eds Kallenbach, R., Geiss, J. and Hartmann, W. K.), Springer, Dordrecht, The Netherlands, 2001, vol. 12, pp. 165–194; https://doi.org/10.1007/978-94-017-1035-0_3.
11. Groshong, R. H., *Geol. Soc., London, Spec. Publ.*, 1996, **99**(1), 79–87; https://doi.org/10.1144/GSL.SP.1996.099.01.07.
12. Borraccini, F., Lanci, L. and Wezel, F. C., *Planet. Space Sci.*, 2006, **54**(7), 701–709; https://doi.org/10.1016/j.pss.2006.03.004.
13. Watters, T. R. and Johnson, C. L., In *Planetary Tectonics* (eds Watters, T. R. and Schultz, R. A.), Cambridge University Press, Cambridge Planetary Science, Cambridge, UK, 2009, pp. 121–182; doi: 10.1017/CBO9780511691645.005.
14. Ruj, T., Komatsu, G., Kawai, K., Okuda, H., Xiao, Z. and Dhingra, D., *Icarus*, 2022, **377**, 114904.
15. Senthil Kumar, P. *et al.*, *J. Geophys. Res.: Planets*, 2016, **121**(2), 147–179.
16. Lena, R., Wöhler, C., Phillips, J., Wirths, M. and Bregante, M. T., *Planet. Space Sci.*, 2007, **55**(10), 1201–1217; https://doi.org/10.1016/j.pss.2007.01.007.
17. French, R. A., Bina, C. R., Robinson, M. S. and Watters, T. R., *Icarus*, 2015, **252**, 95–106; https://doi.org/10.1016/j.icarus.2014.12.031.
18. Head III, J. W. and Wilson, L., *Planet. Space Sci.*, 1993, **41**(10), 719–727; https://doi.org/10.1016/0032-0633(93)90114-H.
19. Wyrick, D., Ferrill, D. A., Morris, A. P., Colton, S. L. and Sims, D. W., *J. Geophys. Res.: Planets*, 2004, **109**(E6); https://doi.org/10.1029/2004JE002240.

ACKNOWLEDGEMENTS. J.T., A.K. and R.B. acknowledge a research grant from the Chandrayaan-2 Science Plan, Space Applications Centre, Kolkata, ISRO, Ahmedabad. We thank Dipayan Dasgupta (Department of Geology, Asutosh College, Kolkata) for help.

Received 8 December 2021; revised accepted 22 April 2022

JOYITA THAPA[1]
ABHIK KUNDU[1,*]
ASHUTOSH ARYA[2]
RWITI BASU[1]

[1]*Department of Geology, Asutosh College, 92, S.P. Mukherjee Road, Kolkata 700 026, India*
[2]*Space Applications Centre, Indian Space Research Organisation, Ahmedabad 380 015, India*
**For correspondence.*
e-mail: kundu.abhik@gmail.com

Air pollution tolerance index of selected roadside plant species in Aizawl, Mizoram, India

AIR pollution tolerance index (APTI) indicates the capability of plant species to mitigate air pollution. Plants purify the air by intercepting particulate matter and smoke, acting as a scavenger for pollutants. The plants sensitive to pollutants act as a pollution bio-indicator. APTI can be helpful in developing appropriate management strategies using plants to minimize the level of air pollutants. The studies on the plant responses to a particular pollutant and APTI based on biochemical parameters are paramount[1,2]. The ability of leaves to intercept dust particles depends on their water holding capacity, chlorophyll content, leaf ascorbic acid content, tree height and canopy[3].

There is ample scope to study plant–pollutant interactions and the absorption of pollutants by plants. Primary pollutants such as sulphur dioxide (SO_2), nitrogen dioxide (NO_2), carbon monoxide (CO) and suspended particulate matter (SPM) enter the plants through stomatal apertures during gaseous exchanges. In the leaves, NO_2 forms nitrous acid which converts ammonia to amino acids and further to proteins[4]. Extensive research has been conducted globally on APTI[1,5–27]. However, there is a paucity of information in Mizoram, North East India. Hence, the present study has been carried out during 2020–21 with an aim to assess the APTI.

Three study sites were selected in the capital of Aizawl in Mizoram. Site-1 (between Sikulpuikawn and Bawngkawn) with heavy traffic, site-2 (New Capital Complex to Khatla) with medium traffic and site-3 (Lalsavunga Park area to Hlimen) with low traffic density. *Mangifera indica*, *Ficus religiosa*, *Ficus benjamina* and *Artocarpus heterophyllus* common at all sites were selected and fully mature leaves were collected in replicates on a seasonal basis for analysis of relative water content[28], pH, ascorbic acid[29], and chlorophyll content[30]. Finally, APTI was calculated using the following formula[31]:

$$\text{APTI} = \frac{A(T+P)+R}{10},$$

where A is the ascorbic acid content (mg/g), T the total chlorophyll content (mg/g), P the pH of leaf extract and R is the relative water content of leaves (%). The plant species were classified as sensitive, tolerant, intermediate and moderately tolerant according to APTI values[9].

Irrespective of the season, there was an increasing trend in relative leaf water content (RWC) from *F. religiosa* to *A. heterophyllus*, *F. benjamina* and *M. indica*, and higher values were reported during monsoon season at all sites. RWC (%) ranged between 51.26 (*F. benjamina* at site-3 in pre-monsoon) and 90.23 (*M. indica* at site-1 in post-monsoon) (Table 1). RWC of trees is the capacity of the leaves to hold water that helps in physiological balance under the stress of air pollution[9,31]. Plants having high RWC denote a high level of tolerance to pollutants[32]. During all the seasons, there was an increasing trend in pH of leaf extract from *F. benjamina*, *A. heterophyllus*, *F. religiosa* and *M. indica*. pH was always in the alkaline range for *M. indica* and acidic for *A. heterophyllus* and *F. benjamina*. The pH value ranged between 5.7 (*F. benjamina* at site-3 in pre-monsoon) and 7.6 (*M. indica* at site-1 in post-monsoon) (Table 2). The decline in leaf pH could be due to decreasing efficiency for converting hexose sugar to ascorbic acid[31,32]. Total chlorophyll content was higher for *M. indica* followed by *A. heterophyllus*, *F. benjamina* and *F. religiosa*. The total chlorophyll content varied between 0.38 (*M. indica* at site-1 in monsoon) and 2.56 (at site-3 in pre-monsoon) (Table 3). Chlorophyll in plants shows photosynthetic activity, growth, accumulation of biomass and health[18,32,33].

The highest value of ascorbic acid (AA) content was reported in *F. benjamina* followed by *F. religiosa*, *M. indica* and *A. heterophyllus* during all seasons and at all sites. The range of AA varied from 0.02 (*A. heterophyllus* at site-1 in pre-monsoon)